Excitation of Sausage Oscillations in a Curved Coronal Loop

by

William Bate

Thesis

Submitted to The University of Warwick

for the degree of

Master of Science

Department of Physics

December 2019

Contents

List of Tables

List of Figures

Acknowledgments

I would like to extend my thanks to the members of the Centre for Fusion, Space and Astrophysics at the University of Warwick. In particular, I would like to thank my supervisor Prof. Valery Nakariakov, Dr. Dmitrii Kolotkov, and Dr. Chris Goddard - for giving me the opportunity to rediscover my love of scientific research, for allowing me to feel comfortable asking the many questions that I have had, and for helping me with all of the practical problems that I have come to you with over my time at Warwick.

Thank you to my friends, Tishtrya Mehta, SJ Spencer, Katarina Blow - for the many different types of fancy hot drinks, for being there for me when I needed someone to talk to, and for being wonderful people who always help to brighten my day.

Thank you to Emma Osbiston for all the support and motivation that you have given me, even from half a continent away, for being a stellar conversation partner, and for always knowing how to put a smile on my face.

Last, but not least, thank you to my incredible family who have never let me down throughout my adventures at university and have always been there for me.

Declarations

This thesis is submitted to the University of Warwick in support of my application for the degree of Master of Science (by Research). It has been composed by myself and has not been submitted in any previous application for any degree. The work presented (including data generated and data analysis) was carried out by the author.

Abstract

This thesis concerns itself with the effects of curvature in the modelling of fast magnetoacoustic sausage oscillations of coronal loops. The Lare2d code was used in order to solve the normalised magnetohydrodynamic (MHD) equations, providing an environment in which the numerical simulations could be performed. An initial plasma set-up was created in order to approximate a coronal loop as a curved magnetic slab. This initial state was then allowed to relax to an equilibrium state, which fast magnetoacoustic sausage oscillations could then be excited in. These oscillations were excited by a velocity pulse and their frequencies and periods measured. A parametric study was conducted by running sixteen numerical experiments with a range of physical parameters in the equilibrium state. The parameters investigated were the minor radius of the curved coronal slab, and the density ratio between the internal and external plasma, with all other properties kept constant. The results of these numerical experiments using a curved slab were then compared with the analytical results for a straight slab with the same properties. Within sufficiently dense and thick slabs, it was found that there was no measurable difference of the period of trapped sausage oscillations between the straight and curved slab models. However, there was a difference of approximately 10% found when modelling trapped sausage oscillations in thicker and less dense curved coronal slabs when compared to the analytical results from the straight slab model. The code used to perform these numerical experiments has been designed to be fully customisable. This is intended to facilitate further studies to be performed that account for the effects of curvature in the modelling of coronal loops.

Abbreviations

AIA	Atmospheric Imaging Assembly.
AMATERAS	Assembly of Metric-band Aperture TElescope and Real-time Analysis System.
BBMS	Badary Broadband Microwave Spectropolarimeter.
CME	Coronal Mass Ejection.
CSHKP	Carmichael, Sturrock, Hirayama, Kopp and Pneuman.
EUV	Extreme Ultraviolet.
FWHM	Full Width at Half Maximum.
IRIS	Interface Region Imaging Spectrograph.
LYRA	Lyman Alpha Radiometer.
MHD	Magnetohydrodynamic.
NRH	Nançay Radioheliograph.
QPPs	Quasi-Periodic Pulsations.
RATAN-600	Academy of Sciences Radio Telescope-600.
SBRS/Huairou	Chinese Solar Broadband Radio Spectrometer at Huairou.
SDO	Solar Dynamics Observatory.
XRT	X-Ray Telescope.

Chapter 1

Introduction

1.1 The Structure of the Sun

The Sun may appear in the sky as a uniform, featureless disc, with its only interesting qualities being providing light and heat to us here on Earth. However, this could not be further from the truth. The solar environment is one which contains many radically different environments. Each have their own physical properties along with processes and events occurring over a huge range of distances and timescales.

The Sun consists of a plasma, mostly made up of hydrogen and helium and it is within the core where these conditions are most extreme. The core of the Sun stretches from its centre out to around 0.25 solar radii, $R_\odot$. Within the core, temperatures reach up to 15.7 MK and pressures are around 25 TPa. These extreme conditions allow nuclear fusion to occur, with hydrogen nuclei fusing together and releasing vast amounts of energy. All of the Sun's energy comes from this process of nuclear fusion, and 99% of this fusion occurs within $0.25R_\odot$ of the centre of the Sun.

This energy is then transferred outwards, and between 0.25 and $0.7R_\odot$ the main vehicle of this energy transfer is through thermal radiation. This gives rise to the name of this region, the radiative zone. The plasma densities within this region fall by a factor of around 100 from 20 g cm^{-3} at its base.

Above this, between 0.7 and $1R_\odot$, the density of the plasma is substantially lower, at approximately 0.2 g cm^{-3}. The temperature gradient is steep enough here for convection flows to occur and as such, this region is known as the convection zone. This convection continues to transfer the energy upwards away from the centre of the Sun, much faster than energy transfer by radiation.

There is no literal solar "surface" of which to speak owing to the fact that the

Sun is comprised of plasma without a true solid surface, meaning that a height must be chosen at which to define the surface of the Sun. This is chosen as the height below which visible light cannot pass and this is where its name derives from, the photosphere. The base of the photosphere is at a height of $1R_{\odot}$ by definition and is much cooler than the core at a temperature of approximately 5800 K. The photosphere extends upwards to a height of $h \approx 400$ km. This lower temperature results in the plasma only having an ionisation of around 3%, meaning that it is mostly comprised of atomic hydrogen.

Much like on Earth, above the surface (or photosphere) the Sun also has an atmosphere, and the region of this solar atmosphere above the photosphere is the chromosphere. Travelling upwards through the chromosphere the density drops from 2×10^{-7} g cm^{-3} to around 1.6×10^{-14} g cm^{-3} at a distance of 2000 km above the photosphere. From the photosphere, progressing up through the chromosphere the temperature first reaches a minimum of $T \sim 4000$ K before rising to around 20000 K at its upper edge.

Just beyond the chromosphere is the transition region which is characterised by large changes in physical parameters over a relatively short change in height. Across a thickness of around 100 km the temperature rises with height by two orders of magnitude up to over 1 MK. This huge, counter-intuitive increase in temperature when travelling away from the energy source (in the core) is known as the coronal heating problem. It is generally agreed that it is caused by the conversion of magnetic energy into other forms of energy, though the mechanism for this is still unknown. Suggestions have included large amounts of nanoflares (see section 1.2.1) and MHD waves (see section 3). The question of the mechanism for this heating is one of the largest unanswered questions within solar physics.

Above the transition region lies the outer atmosphere, known as the corona, which reaches millions of kilometres outwards from the Sun. The plasma within the solar corona is typically at a temperature of 1 to 3 MK, although this can be even higher during some of the events described in Section 1.2. The coronal plasma is highly rarefied, with a density of $\sim 10^{-16}$ g cm^{-3}, although this density varies within some coronal structures. The corona is made up of a magnetically dominated plasma, meaning that the gas pressure is negligible when compared to magnetic pressure, and is almost fully ionised.

1.2 Physical Features of the Solar Corona

The corona is a highly structured environment, with this structure heavily linked to the geometry of the Sun's magnetic field. The overall geometry of this magnetic field can be split into two separate cases which produce different structures and environments.

At the solar poles, the magnetic field can be thought of as approximately unipolar and the field lines open out into space (although of course $\nabla \cdot \mathbf{B} = 0$ is not violated). Regions with this magnetic geometry are generally known as the open corona and they give rise to the high speed solar wind. These areas are also known as coronal holes as they appear dark when observing the corona and this is because the plasma is less dense within coronal holes. Coronal holes are present permanently around the Sun's north and south poles, but can less commonly be found closer to the equator too.

Within coronal holes there are bright, ray-like structures called plumes. These plumes are elongated along the magnetic field and reach heights of several solar radii. The plasma density within these plumes is several times higher than their surroundings and they have widths of a few megametres near the solar surface.

The closed corona is characterised by closed magnetic field lines which connect points of opposite magnetic polarity within the photosphere. Within these regions, the main building blocks of the observed structures are coronal loops. Magnetic flux tubes along these closed field lines can sometimes fill up with plasma which is more hot and more dense than the surroundings, making the magnetic flux tubes visible to observers, and this is what is described as a coronal loop. Typically these coronal loops have lengths of tens or hundreds of megametres and minor radii of up to several megametres.

The two points where the loop enters the photosphere are known as the footpoints of the loop and are anchored to the solar surface. The footpoints of a coronal loop are at positions with a high concentration of magnetic flux. Sometimes, though not always, the strong magnetic flux can weaken and divert the convection flows that move hot plasma up to the photosphere. This can result in the footpoints of a coronal loop being cooler than the surrounding photosphere, appearing darker, and these regions are known as sunspots.

Coronal loops are brighter than their surroundings due to having higher densities than the plasma around them. Coronal loops can oscillate in many different ways, described in section 3 and this, coupled with their brightness compared to the corona surrounding them, makes them ideal candidates to observe in order to learn more about the processes occurring within solar plasmas.

A filament (or prominence) is a structure that lies above the neutral line of a

bipolar system in the solar corona. These structures are filled in with much cooler plasma than the surrounding corona, usually at temperatures of around 50000 K, similar to the plasma in the chromosphere. It is important to note that filaments and prominences are in fact the same phenomena, just viewed in different environments. Due to their lower temperatures they appear dark compared to the bright background when viewed in EUV against the solar disk and here they are known as filaments. However, when viewed above the limb they appear bright against the dark background and are known as prominences.

Active regions are areas of extremely high magnetic field strength, at around $1000 - 3000$ G or up to 1000 times the background magnetic field with many closed field lines. These active regions are environments with a lot of magnetic activity, resulting in many dynamic processes. One of these dynamic processes is plasma heating within the chromosphere, allowing plasma to evaporate upwards along magnetic field lines and fill in flux tubes to create coronal loops. This is why active regions typically are home to many coronal loops.

1.2.1 Eruptive Phenomena

The main driver for eruptive events within the solar corona is magnetic reconnection. Reconnection most often, but not always, happens as a violent and short lived process. When the coronal magnetic field is put under large amounts of stress it can result in the large scale restructuring of the magnetic field through topological changes. These topological changes cause the liberation of large amounts of energy which results in plasma heating, particle acceleration and kinematic motion of the plasma.

A solar flare is a rapid release of energy within the solar corona, associated with magnetic reconnection. Solar flares emit huge amounts of radiation in almost all wavelengths, ranging from radio up to even gamma rays for some of the largest events. The amount of energy released varies across many orders of magnitude and microflares (with energies of 10^{-6} times those of the largest flares) are even observed outside of active regions, within the quiet-Sun environment. Solar flares can sometimes occur within systems of multiple coronal loops due to the high magnetic field stresses present within these structures.

The standard model of solar flares is known as the Carmichael, Sturrock, Hirayama, Kopp and Pneuman (CSHKP) model and is illustrated in figure 1.1. This begins with a filament forming above the neutral line of a closed bipolar magnetic field, filled in with cool, dense plasma. This causes the closed magnetic field to evolve into

a non-equilibrium state where the magnetic field lines open out and the filament is erupted upwards. Magnetic reconnection then occurs below the filament which is traveling outwards. It is this magnetic reconnection that provides plasma heating and particle acceleration and is known as the flare.

The precipitation of these energised particles downwards along the magnetic field lines causes radio emission. When these particles hit the chromosphere hard X-ray and Hydrogen-α emission is produced. These energetic particles then heat the chromosphere and cause some of the chromospheric plasma to evaporate upwards along the magnetic field lines causing soft X-ray emission.

A Coronal Mass Ejection (CME) is an expulsion of plasma from the solar corona. These events often occur in relation with large solar flares and result in large amounts of plasma, with an associated magnetic flux, travelling outwards into the solar system and expanding in size as they travel.

It is important to note that different wavelengths of radiation are produced at different positions and times during a solar flare, and that both open and closed coronal magnetic fields are important within their evolution.

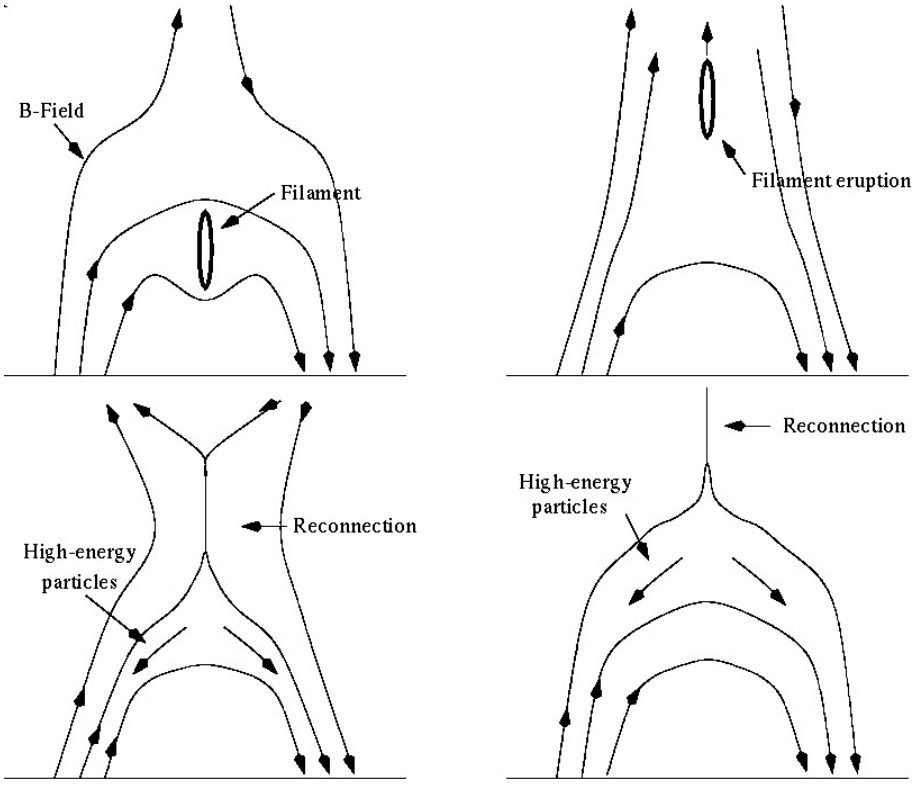

Figure 1.1: The standard CSHKP 2D reconnection model for solar flares.

1.3 Motivation for Studying the Solar Corona

The solar wind is an ever present stream of plasma being released from the corona and travelling away from the Sun in all directions. This solar wind has different speeds depending on a number of factors, with most noticeable factor being latitude. This is because the charged particles that make up the plasma can travel along the open magnetic field lines present in these open corona regions. As a result, the fast solar wind is emitted from the open corona at speeds of approximately 750 km s^{-1} and with a temperature of ~ 0.1 MK.

Conversely, the slow solar wind is emitted from the closed corona and travels at speeds of $300-500$ km s^{-1} with a temperature of 0.8 MK and a density of around half as high as the fast solar wind. As all the planets in the solar system travel very close to the plane of the ecliptic, the vast majority of the time it is this slow solar wind that reaches and interacts with the planets. It is this interaction between the Earth's magnetic field and the the charged particles arriving in the plasma of the solar wind that causes the aurorae.

However, variations in conditions in the solar atmosphere can cause large changes in this interaction between the solar and geomagnetic fields. For example, if a coronal hole were to manifest itself in the correct position, close to the equator, then the Earth's magnetic field would be exposed to the fast solar wind. This causes a disturbance to the magnetic field known as a geomagnetic storm.

Even larger geomagnetic storms can be caused by the plasma ejected from a CME travelling towards and interacting with Earth. The largest recorded geomagnetic storm occurred on 1st-2nd September 1859 and is known as the Carrington Event. This was caused by an extremely large CME and resulted in aurorae being observed as far south as Cuba and telegraph wires caught fire and delivered shocks to their operators. It was estimated in 2010 that a similar event in modern times would have an economic cost of 0.6-2.6 trillion USD to the United States alone. [Hapgood & Thomson, 2010]

As such, it is imperative that the processes that govern solar plasma and the associated phenomena continue to be researched and better understood. To that end, the solar atmosphere is the best plasma experiment currently possible. It is able to be observed constantly and has been for decades at higher temporal and spatial resolutions over time. Plasma based experiments are notoriously difficult to create on Earth, but there is a huge-scale, constantly running experiment on our astronomical doorstep.

Due to the Sun being the only star that can be spatially resolved, it is enormously important in understanding stellar observations too. Observations of stars come in the

form of electromagnetic flux emitted from a point, so by integrating over the full area of the Sun similar readings for our Sun can be produced. Comparing the data from these "Sun as a star" experiments to the spatially resolved data we have from the Sun allows us to much better interpret the data received from observational experiments on other stars.

Chapter 2

Observations

2.1 Quasi-Periodic Pulsations

Quasi-Periodic Pulsations (QPPs) are one of the most common features seen in light curves of solar and stellar flares. This means that understanding mechanisms that can produce QPPs is very important in analysing these light curves. By analysing these QPPs we can often learn a lot about the physical parameters in the environment of a flare, as well as the flare's time evolution.

These QPPs are observed in all wavelengths of the electromagnetic spectrum and are often close to synchronous in all of these emission bands. However, what makes these oscillations "quasi-periodic" is the instability or time modulation of their oscillatory periods. It is also very common to see amplitude-modulation of QPPs and they can have periods of anywhere from less than a second to hundreds of seconds. Due to the extremely high intensity of the emission from flaring events, these observations are able to have high time resolutions compared to other methods of observation.

There are many mechanisms which can produce QPPs in observed emissions, but the mechanism most closely associated to the topic of this thesis is the modulation of plasma parameters by Magnetohydrodynamic (MHD) oscillations which are discussed further in section 3. Within solar flares (discussed in more detail in section 1.2.1) electrons are accelerated to an appreciable fraction of the speed of light. These electrons emit gyrosynchotron radiation and it is this radiation that is responsible for the large amounts of radio waves produced by solar flares.

Three of the main plasma parameters that affect the intensity of gyrosynchotron radiation, I, are the magnetic field, B; the angle of the magnetic field to the line of sight, θ; and the electron density, n_e. As is discussed in more detail by Nakariakov et al.

[2016], in the optically thin regime the radiation intensity is particularly sensitive to changes in magnetic field strength. For typical coronal parameters the proportionality can be around $I \propto B^{3.4}$ meaning that even small changes in the magnetic field can cause significant changes in observed intensity. This is particularly important for MHD sausage oscillations which modulate the magnetic field strength and as such modulate the observed signal. MHD kink or torsional standing modes and propogating waves can modulate θ, which in the optically thin regime and for typical coronal plasma parameters has a relationship with intensity of $I \propto (\sin\theta)^{3.57}$. This means that the amplitude of these oscillations is also amplified in the oscillations of intensity. Slow magnetoacoustic modes can also produce oscillations in intensity through modulation of the plasma density causing modulation of n_e.

Consequently, the MHD modes of coronal structures (see section 3.2) and Alfvén, or torsional, waves can produce QPPs in the radio emission from solar flares, which often have much higher amplitudes than those of the physical oscillations themselves. Mossessian & Fleishman [2012] investigated how one would tell the difference between QPPs produced by different MHD modes within coronal structures. This investigation was performed by perturbing the magnetic field vector in order to simulate these different MHD modes. For the sausage mode oscillation it was found that the intensity oscillations had a phase difference of π between high and low emission frequencies. Also, at high and low frequencies the flux is in phase with the degree of polarisation. For kink mode oscillations it was found that there was no phase change at different observational frequencies. This allows for QPPs produced by different MHD modes to be distinguished between.

2.2 Examples of Spatially Resolved QPPs

Observations of sausage modes within coronal loops have been relatively sporadic in comparison to those of kink modes for example. This can be attributed to two main factors, the first is the insufficient time resolution of Extreme Ultraviolet (EUV) telescopes that are currently in use. Melnikov et al. attributed 16 s and 9.5 s period oscillations in microwave radiation to the sausage oscillations of a coronal loop, however the Atmospheric Imaging Assembly (AIA) on Solar Dynamics Observatory (SDO) only has a time resolution of 12 s, making observations difficult.

The second and most important factor is the fact that the sausage mode perturbs plasma in the radial direction coupled with the pixel size available for most available EUV instruments. In the optically thin regime, which describes the solar corona well,

thermal emission is given by the following,

$$\mathrm{I}(t) \propto \iint_{pixel} dA \int_{LoS} \rho^2(t) ds, \tag{2.1}$$

where $\mathrm{I}(t)$ is the intensity of the thermal emission, $\rho(t)$ is density, the inner integral is along the line of sight and the outer integral is across our pixel in the plane of the sky. As the plasma is perturbed radially, if the pixel size is larger or similarly sized to the coronal loop being imaged, the same plasma stays inside the same pixel and along our line of sight. This means that the amplitude of the observed intensity oscillation is significantly lower than that of the wave itself. This problem can be lessened by taking observations where the line of sight is not perpendicular to the axis of the coronal loop at a point. [Cooper et al., 2003] [Antolin & Van Doorsselaere, 2013]

Gruszecki et al. [2012] examined the observed intensity oscillations due to sausage modes within a cylindrical coronal loop for different pixel sizes. It was found that when the pixel size was the same width as the plasma cylinder, the change in observed intensity is proportional to the relative physical change squared. This means that for an oscillation with the amplitude 3%, the observed intensity oscillation only has an amplitude of 0.09%. As a result, variations in the emission intensity in the optically thin regime due to sausage oscillations are not always of a detectable level when the oscillating structure is not well resolved.

Owing to these difficulties in observation of sausage oscillations in coronal loops there are few observational detections and some are given below, with their main properties and detection methods.

Tian et al. [2016] used oscillations in both the intensity and Doppler shift in the Fe_{XXI} line as measured by Interface Region Imaging Spectrograph (IRIS), as well as in the soft X-ray flux intensity recorded by GOES. A phase difference of $\sim \pi/4$ between the Doppler shift and intensity allowed these 25 s period oscillations to be interpreted as global sausage oscillations of the coronal loop. They were also able to prescribe a lower bound for the density contrast of $\rho_0/\rho_e \geq 42$, where ρ_0 is the density inside the coronal loop, and ρ_e is the density of the surrounding plasma.

Mészárosová et al. [2016] observed a microwave event which occurred during a solar flare in the broadband microwave emission at around 1 GHz using Badary Broadband Microwave Spectropolarimeter (BBMS). By performing wavelet analysis on the separated dynamic radio spectra from this event, clear tadpole patterns were observed which are a key sign of propagating sausage mode oscillations. Two wavelet tadpole patterns were found, the first with a period of ≈ 0.7 s and a frequency drift of 2892 MHz s^{-1};

the second with a period of ≈ 2 s and no measurable frequency drift.

Carley et al. [2019] observed high intensity bursts of radio emission during a solar flare using Orfées (208 MHz) and Nançay Radioheliograph (NRH) (228 MHz). This pulsating radio source was found to have a period of 2.3 s and a coronal loop was identified using SDO/AIA that could have contained this oscillation. The identified coronal loop had a length of $L \approx 35$ Mm; a minor radius of $a = 2.5 - 5.5$ Mm; an elctron density of $n_e = 1.7 - 2.7 \times 10^9$ cm^{-3}; and a temperature of $T = 1 - 1.6$ MK. These oscillations were identified as sausage mode oscillations and the emission mechanism was proposed as the modulation of electron acceleration within the coronal loop caused by a loss-cone instability which is associated with a sausage oscillation.

2.3 Examples of Spatially Unresolved QPPs

Analysis of light curves from a coronal event can be used to glean information about the structures and types of oscillations that were present. This allows for useful diagnostics of plasma and oscillation parameters without the structures or oscillations themselves being spatially resolved.

Van Doorsselaere et al. [2011] were able to identify both long (~ 75 s) and short (~ 8.5 s) period oscillations within an single, unresolved flare. These observations were made in the Lyman-α line using the Lyman Alpha Radiometer (LYRA) instrument. These oscillations were interpreted as the standing slow sausage mode and the standing fast sausage mode respectively within the flaring loop. Due to having observed two modes within the same structure, more detailed seismology was able to be conducted giving a maximum density contrast of $\rho_0/\rho_e \leq 18$ and a minimum internal plasma-β of 0.016. Combining this with data from Hinode/X-Ray Telescope (XRT), a value for the aspect ratio of the structure, $L/2a = 4.6$, was calculated.

Yu et al. [2013] found quasi-periodic wiggles when analysing the zebra pattern of an unresolved flare event with data taken from Chinese Solar Broadband Radio Spectrometer at Huairou (SBRS/Huairou). From these zebra pattern structures, some properties of the oscillating structure and these oscillations could be estimated. These properties were two or three periods of $0.5 - 1.5$ s; an Alfvén speed of $C_A \sim 700$ km s^{-1}; a spatial scale of $2a \sim 1$ Mm; and a magnetic field strength of 50 G. Due to the wiggles in different stripes within the zebra pattern being roughly in phase, it was concluded that they were due to a standing sausage oscillation.

Kaneda et al. [2018] used Assembly of Metric-band Aperture TElescope and Real-time Analysis System (AMATERAS) to observe a unresolved solar flare during which

several solar radio bursts occurred, one of which produced a zebra pattern. The frequency difference between neighbouring stripes, Δf, was found to be quasi-periodically modulated with a period of $1-2$ s and a frequency drift rate of $3-8$ MHz s^{-1}. The cause of this modulation was found to have a spatial scale of 7.7 Mm and was propagating along the coronal loop with a phase speed of $3000-8000$ km s^{-1}. It was concluded that this modulation of Δf was due to propagating fast sausage mode oscillations.

Nakariakov et al. [2018] observed the time evolution of radio emission from a microflare using Academy of Sciences Radio Telescope-600 (RATAN-600). This radio wavelength emission was associated with non-thermal electrons and was produced at both footpoints of a coronal loop structure, both observed simultaneously. 1.4 s QPPs were detected in both the left and right polarisation along with a 0.7 s QPP observed in the difference between them. This allowed the mechanism for their creation to be interpreted as the superposition of the fundamental and second harmonic of a sausage mode oscillation within the coronal loop.

Chapter 3

MHD Modes of Plasma Non-Uniformities

3.1 Ideal Magnetohydrodynamics

Numerical simulations are extremely powerful tools in the study of plasma physics. Their use in any field relies on a solid mathematical model that provides a good approximation of the physical reality. Within plasma physics, MHD is the most commonly used theory in modelling.

MHD is a method of modelling plasma as an electrically conducting fluid. It describes the large scale, slow motion of plasmas. In more certain terms, it can be used to model plasmas under the following three conditions: characteristic scale $\gg$ ion gyroperiod and mean free path time; characteristic length $\gg$ ion gyroradius and mean free path length; the velocities are non-relativistic.

Within the solar corona the characteristic length scale is of the order 10^6 m and the mean free path length, $\lambda \sim 10^5$ m. The characteristic time scales of the oscillations $\sim 10^2$ s and the ion gyroperiod $\sim 10^{-4}$ s. Finally, the velocities within the corona are of the order of magnitude of thousands of km s^{-1}, so are non-relativistic. This means that MHD is applicable within the solar corona and within the hot coronal loops that we will be modelling.

The governing equations of ideal MHD (neglecting all dissipative effects from viscosity, electrical resistivity and thermal conductivity) are as follows:

$$\frac{\partial \rho}{\partial t} + \nabla(\rho \mathbf{u}) = 0, \tag{3.1}$$

$$\frac{\mathrm{d}}{\mathrm{d}t}\left(\frac{P}{\rho^{\gamma}}\right) = 0, \tag{3.2}$$

$$\rho\left(\frac{\partial \mathbf{u}}{\partial t} + (\mathbf{u}\cdot\nabla)\mathbf{u}\right) = -\nabla P - \frac{1}{\mu_0}\mathbf{B}\times(\nabla\times\mathbf{B}), \tag{3.3}$$

$$\frac{\partial \mathbf{B}}{\partial t} = \nabla\times(\mathbf{u}\times\mathbf{B}), \tag{3.4}$$

where ρ is the plasma density, t is time, $\mathbf{u}$ is the bulk flow velocity, P is the plasma pressure, γ is the adiabatic index, μ_0 is the permeability of free space and $\mathbf{B}$ is the magnetic field.

Additionally, the magnetic field is subject to the condition

$$\nabla\cdot\mathbf{B} = 0. \tag{3.5}$$

If we consider a static equilibrium case with a characteristic scale, λ, and the conditions

$$\mathbf{u} = 0, \frac{\partial}{\partial t} = 0, \tag{3.6}$$

and examine equation 3.3, then we are left with two terms: the gas pressure gradient, $\nabla P \sim P/\lambda$, and the Lorentz force, $\frac{1}{\mu_0}\mathbf{B}\times(\nabla\times\mathbf{B}) \sim B^2/(\mu_0\lambda)$. The ratio of the gas pressure gradient and the Lorentz force is the defined as the plasma-β,

$$\beta \equiv \frac{\text{gas pressure}}{\text{magnetic pressure}} = \frac{P}{B^2/2\mu_0}. \tag{3.7}$$

If these governing equations of MHD are linearised within a uniform medium then we find that there are three forms of solutions (modes), each with characteristic properties and a characteristic speed. The Alfvén mode is essentially incompressive and the fast and slow magnetoacoustic modes both essentially compressive. All of these MHD modes are dispersionless within a uniform medium. It is useful to introduce some characteristic speeds of these MHD modes: the Alfvén speed, $C_A = B_0/(\mu_0\rho_0)^{\frac{1}{2}}$, where B_0 is the unpeturbed value of the magnetic field and ρ_0 is the unperturbed density; and the sound speed, $C_s = (\gamma P_0/\rho_0)^{\frac{1}{2}}$, where P_0 is the unperturbed pressure.

These MHD waves are anisotropic and heavily depend on their angle, α, to the magnetic field. In a low β plasma ($\beta < 1$), when $\alpha = 0$, the Alfvén waves have phase speed C_A; the slow magnetoacoustic waves have phase speed C_s; and the fast magnetoacoustic waves have phase speed C_A and become incompressive. As we increase the

angle until $\alpha = \pi/2$, the phase speed of the Alfvén waves decreases to 0; the phase speed of the slow magnetoacoustic waves decreases to 0; and the phase speed of the fast magnetoacoustic waves increases to the fast phase speed, $C_f = (C_A^2 + C_s^2)^{\frac{1}{2}}$.

3.2 MHD modes of a straight cylinder

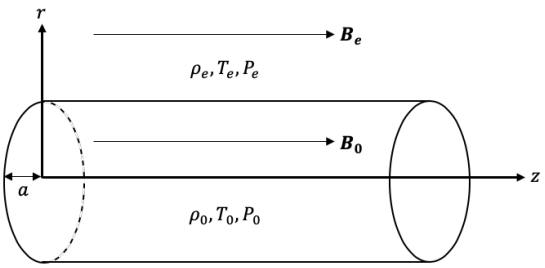

Figure 3.1: A magnetic flux tube of radius a embedded in a magnetised plasma.

This idealised case of a uniform medium is not appropriate to describe the decidedly non-uniform solar corona and these results are significantly altered when non-uniformities are introduced. To model an axisymmetric plasma structure, such as a coronal loop, we will consider the case shown in Figure 3.1. It is mathematically useful here to introduce the tube speed, $C_T = C_s C_A/(C_A^2 + C_s^2)^{\frac{1}{2}}$, which is the group speed of a slow magnetoacoustic mode oblique to a magnetic field.

Consider a straight cylindrical magnetic flux tube directed along the z-axis with radius a. Inside the flux tube is a uniform plasma with properties given the subscript 0 (ρ_0, P_0 and T_0 are the internal density, pressure and temperature respectively) and an internal magnetic field, $\mathbf{B_0}$, in the z-direction. Outside of this cylider there is also a uniform plasma with properties given the subscript e (ρ_e, P_e and T_e are the external density, pressure and temperature respectively) and a similar external magnetic field, $\mathbf{B_e}$, in the z-direction. The internal and external Alfvén speeds are C_{A0} and C_{Ae} respectively; the internal and external sound speeds are C_{S0} and C_{Se} respectively; and the internal and external tube speeds are C_{T0} and C_{Te} respectively.

For this equilibrium setup to exist, the total pressure, P_{tot}, must be balanced internally and externally, resulting in the condition

$$P_0 + \frac{B_0^2}{2\mu_0} = P_e + \frac{B_e^2}{2\mu_0}. \tag{3.8}$$

If the MHD equations are linearised around this equilibrium by using linear perturbations of the form $\delta P_{\rm tot}(r)\exp[\imath(k_z z + m\phi - \omega t)]$ (where k_z is the parallel wavenumber, the integer m is the azimuthal wave number and ω is the frequency) we find the dispersion relations for the internal and external media:

$$(\omega^2 - C_{A\alpha}^2 k_z^2)\left[\frac{\mathrm{d}^2}{\mathrm{d}r^2} + \frac{1}{r}\frac{\mathrm{d}}{\mathrm{d}r} - \left(\kappa_\alpha^2 + \frac{m^2}{r^2}\right)\right]\delta P_{\rm tot} = 0, \tag{3.9}$$

where

$$\kappa_\alpha^2(\omega) = \frac{(k_z^2 C_{s\alpha}^2 - \omega^2)(k_z^2 C_{A\alpha}^2 - \omega^2)}{(C_{s\alpha}^2 + C_{A\alpha}^2)(k_z^2 C_{T\alpha}^2 - \omega^2)}, \tag{3.10}$$

and $\alpha = 0, e$.

The first term of equation (3.9) represents torsional Alfvén waves with dispersion relations of the form $\omega = \pm C_{A\alpha} k_z$. Examining the second term results in a Bessel-like equation describing magnetoacoustic modes. Boundary conditions need to be applied in order to solve this equation and these are the jump conditions (continuity of total pressure and normal velocity). In the case of a steady flow, the continuity of transverse velocity can be considered as the continuity of transverse displacement. Applying these boundary conditions, we arrive at the dispersion relation:

$$\rho_e(\omega^2 - k_z^2 C_{Ae}^2)\kappa_0 \frac{I_m'(\kappa_0 a)}{I_m(\kappa_0 a)} + \rho_0(k_z^2 C_{A0}^2 - \omega^2)\kappa_e \frac{K_m'(\kappa_e a)}{K_m(\kappa_e a)} = 0, \tag{3.11}$$

where $\kappa_{0,e}$ are the internal and external transverse wavenumbers respectively, given by equation (3.10); $I_m(x)$ and $K_m(x)$ are modified Bessel functions with order m; and $I_m'(x) = \frac{\mathrm{d}I_m(x)}{\mathrm{d}x}$ and $K_m'(x) = \frac{\mathrm{d}K_m(x)}{\mathrm{d}x}$ are their derivatives with respect to their arguments. [Edwin & Roberts, 1983]

There are two separate cases possible given the dispersion relation in equation (3.11), either $\kappa_e^2 > 0$, which corresponds to modes which are confined to the cylinder and are evanescent outside - known as trapped modes, or $\kappa_e^2 < 0$, which corresponds to modes which are oscillatory outside the cylinder - known as leaky modes.

If we consider only the trapped modes of the cylinder (by imposing the condition $\kappa_{0,e} > 0$), the azimuthal wavenumber, m, determines the azimuthal structure, with $m = 0$ corresponding to sausage modes, $m = \pm 1$ corresponding to kink modes and $|m| > 2$ corresponding to flute or ballooning modes.

When allowing waves to radiate outside the cylinder and examining the leaky modes, the dispersion relation given in equation (3.11) needs to be modified. This is achieved by replacing the modified Bessel functions with Hankel functions.

3.3 Magnetic Slab

Figure 3.2 plots the phase speed of trapped modes as a function of normalised wavenumber. The solid lines respresent the 2D slab model Edwin & Roberts [1982] and the dashed lines represent the 3D cylindrical model Edwin & Roberts [1983]. It is evident from the left panel that the sausage mode is much less dependant on the choice of geometry when compared to the kink mode shown in the right panel. This allows us to use a 2D or 2.5D model when modelling sausage modes, without a large loss in accuracy.

For both the slab and cylindrical models the phase speed of these trapped sausage modes has two limiting values: a lower bound of C_{A0} when $ka \to \infty$; and an upper bound of C_{Ae} at $k_c a$, where we have defined a cut-off wavenumber k_c.

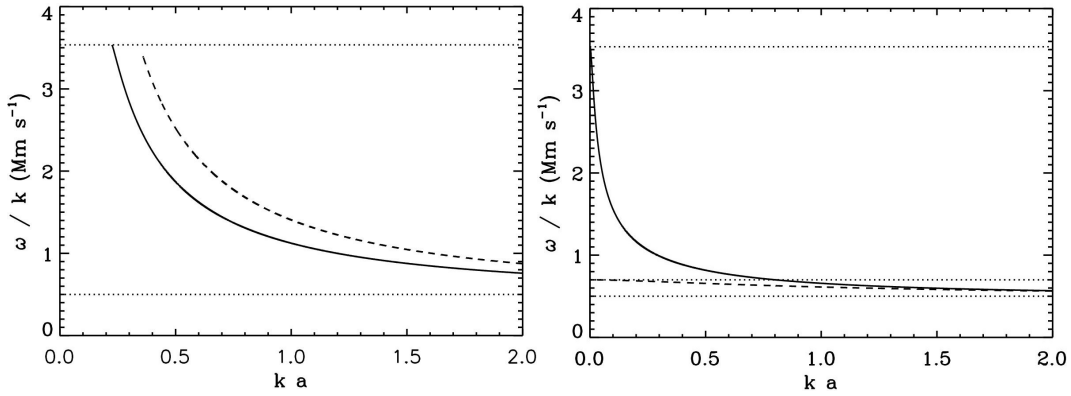

Figure 3.2: Phase speed $\frac{\omega}{k}$ as a function of normalised wavenumber ka for the trapped sausage (left) and kink (right) modes in a loop with density contrast $\rho_0/\rho_e = 50$ (and plasma-$\beta = 0$). The solid lines are for the slab geometry and the dashed lines are for the cylindrical geometry. The lower and upper dotted lines correspond to the internal Alfvén speed C_{A0} and external Alfvén speed C_{Ae}, respectively. In the right panel the middle dotted line corresponds to the kink speed c_k. [Pascoe & Nakariakov, 2016]

In the case of the cross sectional density being taken as a step function with width $2a$, the wave equation gives rise to the dispersion relation

$$\tan\left(\frac{\omega^2}{C_{A0}^2} - k^2\right)^{1/2} a = -\left(\frac{\omega^2/C_{A0}^2 - k}{k^2 - \omega^2/C_{Ae}^2}\right)^{1/2} \tag{3.12}$$

for trapped sausage mode oscillations.

Examining this dispersion relation gives rise to some conditions for solutions with real values of k and ω, namely $C_{Ae} > C_{A0}$ and $C_{A0} < \omega/k < C_{Ae}$. Furthermore, it can be seen that there is a cut-off wavenumber, k_c, below which trapped sausage oscillations cannot occur where

$$k_c a = \frac{\pi}{2}\left(\frac{C_{A0}^2}{C_{Ae}^2 - C_{A0}^2}\right)^{1/2}. \tag{3.13}$$

Another case to consider is one where the cross sectional density is of the form given below, referred to as an Epstein profile, which allows the dispersion relation to be solved analytically. The Epstein profile is defined as

$$\rho\left(\frac{x}{a}\right) = (\rho_0 - \rho_e)\,\mathrm{sech}^2\left(\frac{x}{a}\right) + \rho_e, \tag{3.14}$$

where ρ_0 is the maximum value of the density (when $x/a = 0$); and ρ_e is the minimum value of the density (when $x/a \to \infty$).

This gives the dispersion relation for trapped sausage mode oscillations as

$$(ka)^2\left(\frac{\omega/k}{C_{A0}^2} - 1\right) - 2 = 3(ka)\sqrt{1 - \frac{(\omega/k)^2}{C_{Ae}^2}}, \tag{3.15}$$

which can be solved for our normalised phase speed, $\frac{\omega/k}{C_{A0}}$, as follows:

$$\left(\frac{\omega/k}{C_{A0}}\right)^2 = \frac{1}{2(ka)^2}\left(2(ka)^2 + 4 - \frac{9}{b} + 3\sqrt{\frac{9}{b^2} - \frac{4(ka)^2}{b} - \frac{8}{b} + 4(ka)^2}\right), \tag{3.16}$$

where $b = (C_{Ae}/C_{A0})^2 = \rho_0/\rho_e$ is our density contrast.

From equation 3.15 we can find the cut-off value for the normalised wavenumber, achieved by setting $(\omega/k)^2 = C_{Ae}^2$,

$$k_c a = \left(\frac{2C_{A0}^2}{C_{Ae}^2 - C_{A0}^2}\right)^{1/2}, \tag{3.17}$$

and ka must exceed this cut-off value in order for global sausage mode oscillations to occur.

The fact that this cut-off wavenumber, k_c, exists in both of these cases means that in order to observe trapped global sausage mode oscillations for a significant number of cycles then the coronal loop must be sufficiently thick and dense.

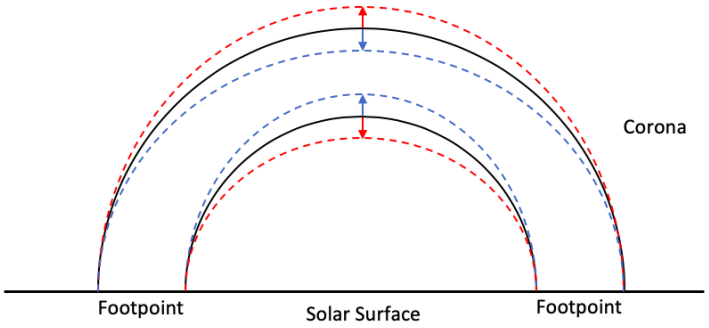

Figure 3.3: The sausage mode of a coronal loop is an anti-symmetric perturbation to the transverse velocity profile of the loop, causing the variation of the loop minor radius and hence the subsequent contractions (dashed blue curves) and widenings (dashed red curves) of the loop around an equilibrium (solid black curves). This mode does not perturb the axis of the coronal loop.

3.4 Previous Modelling of Sausage Modes

Inglis et al. [2009] modelled a coronal loop as a straight magnetic slab with a cross sectional density set as an Epstein profile, described by equation 3.14. Plasma-β was varied across the cross section of the structure, having a constant small external value, β_e, and a variable peak internal value, β_0. β_0 was adjusted by changing the internal magnetic field strength. When β_0 was varied between 0.01 and 1.5 the period of the global trapped sausage mode was found to have a very weak positive dependence on β_0, with a variation of $< 5\%$.

The cut-off wavenumber, k_c, was also examined when varying β_0 for fixed values of the density contrast, ρ_0/ρ_e. This was performed both analytically and with numerical simulations. It was found that for a fixed density contrast, k_c had a negative dependence on β_0 although again this variation was relatively small. However, any changes in density contrast were found to have a large effect on k_c, with higher density contrasts resulting in lower cut-off wavenumbers. This indicates that density contrast has a large effect on sausage mode confinement.

The harmonic ratio was also studied for the fundamental and second harmonic modes. The value of $k_1 a$ was varied and $P_1/2P_2$ was measured, where k_1 is the wavenumber of the fundamental mode; P_1 is the period of the fundamental mode; and P_2 is the period of the second harmonic mode. A numerical simulation was performed for a fixed density contrast and the harmonic ratio was found to increase between 0.6 and 0.8 for increasing values of $k_1 a$ between 0.4 and 2. This harmonic ratio of non-dispersive waves is

expected to have a value of 1 and this deviation indicates how the dispersion of sausage modes depends on wavenumber. Using the analytical expressions it was shown that density contrast has a strong effect on the harmonic ratio, with larger density contrasts producing greater deviations from the ideal, non-dispersive value of 1. The harmonic ratio was found to lie between 0.5 and 1 for all cases.

Chen et al. [2015] produced a numerical parametric study of a cylindrical coronal loop to examine the effects of the radial structure of the density on the period and damping time of sausage oscillations. This loop was modelled as a cylinder with its axis in the z-direction with a uniform magnetic field in the z-direction. Cold MHD (plasma-$\beta = 0$) was assumed.

The density profile was set as

$$\rho = \rho_e + (\rho_i - \rho_e) \exp\Big[-(\frac{r}{a})^q\Big] + \rho_{\mathrm{FS}}(r), \qquad q > 1, \tag{3.18}$$

where q is a steepness parameter and $\rho_{\mathrm{FS}}(r)$ is a term which describes the fine structuring of the density. When $q = 2$ and $\rho_{\mathrm{FS}}(r) = 0$, this density profile is similar to the symmetric Epstein profile described by equation 3.14. When keeping $q = 2$ and introducing a periodic fine structuring with n concentric shells it was found that for all $n >= 3$ the fractional change in period and damping time in the small wavelength limit compared to the monolithic case, δP and $\delta\tau$ respectively, was less than 1%. Then the case was considered where $q = 2$ and random fine structuring was introduced by summing N different random sinusoids. It was found that for $N >= 10$ the deviations from the monolithic case were $\delta P < 2\%$ and $\delta\tau < 10\%$. This means that, assuming coronal loops are made up of a sufficiently large number of fine structures, the major observables of sausage oscillations, period and damping time, are affected by fine structuring at rates much lower than observational uncertainties. This means that it is acceptable to neglect the fine structure of the density profile when modelling sausage oscillations within coronal loops.

The effect of the steepness of the density profile was investigated, which is characterised by the parameter q similarly to the Epstein profile in figure 4.2. When q was increased from 2 to 100 in the small wavenumber limit, the period remained relatively constant but the damping time grew by a factor of ~ 2. This change due to the steepness parameter is much more prominent than the effects due to fine structuring.

Pascoe & Nakariakov [2016] modelled a sausage mode oscillations within curved coronal loops and investigated the effect of different properties of the numerical set up on the properties of sausage mode oscillations within the structure. Their set up involved

a potential magnetic field and a low, but non-zero, internal plasma-$\beta = \beta_0$. The density profile used was based on the symmetric Epstein profile, described by equation 4.5, but heavily modified to include curvature along the magnetic field lines; an increase in a at the top of the loop; and vertical stratification described by a scale height, Λ.

As Λ was increased from 0.5 to 2 it was found that the periods of the fundamental (P_1), second harmonic (P_2), and third harmonic (P_3) all increased, with P_1 increasing from 15 s to 25 s. However, when examining the harmonic ratios for the second and third harmonics, $P_1/2P_2$ and $P_1/3P_3$ respectively, it was found that these both remained approximately constant. It was also found that this model of an expanding, curved coronal loop resulted in an increase to the harmonic ratios when compared to a straight slab model of a coronal loop.

Chapter 4

Simulations

4.1 Lare

In order to solve these equations computationally, and to produce numerical simulations, the LareXd codes have been used. More specifically, Lare2d has been used, which is a Lagrangian remap code for solving the MHD equations in 2D. [Arber et al., 2001]

The code solves normalised MHD equations with the normalising constants for length, magnetic field strength and density ($\widetilde{L}$, $\widetilde{B}$ and $\widetilde{\rho}$) initially set by the user. All other normalisation constants are defined in terms of these three user specified cases. The average mass for ions within the plasma must also be set, which is treated throughout this work as $\bar{m} = 1.2m_p$, where m_p is the proton mass. The code includes the effects of viscosity, resistivity and conductivity, however these will be neglected for the purposes of this investigation.

The normalised, ideal MHD equations can then be derived from equations 3.1 - 3.4 as

$$\frac{D\rho}{Dt} = -\rho\nabla\cdot\mathbf{u}, \tag{4.1}$$

$$\rho\frac{D\mathbf{u}}{Dt} = (\nabla\times\mathbf{B})\times\mathbf{B} - \nabla P, \tag{4.2}$$

$$\frac{D\mathbf{B}}{Dt} = (\mathbf{B}\cdot\nabla)\mathbf{u} - \mathbf{B}(\nabla\cdot\mathbf{u}), \tag{4.3}$$

$$\rho\frac{D\epsilon}{Dt} = -P\nabla\cdot\mathbf{u}, \tag{4.4}$$

where $\epsilon = P/\rho(\gamma - 1)$ is the internal energy density.

Lare2d employs a staggered grid in order to avoid the checkerboard instability. [Sigmund & Petersson, 1998]. This means that variables within the code are defined at different points within the computational cell. Scalars and B_z are defined at the cell centres; B_x and B_y are defined at the cell boundaries; and velocities are defined at the cell vertices, as shown in figure 4.1. In order to utilise variables defined at different places within the cell, for example when calculating kinetic energy, one must take great care to find their values at the same point. For example, this can be done to find the density at a cell vertex by averaging the density at the centres of the four surrounding cells.

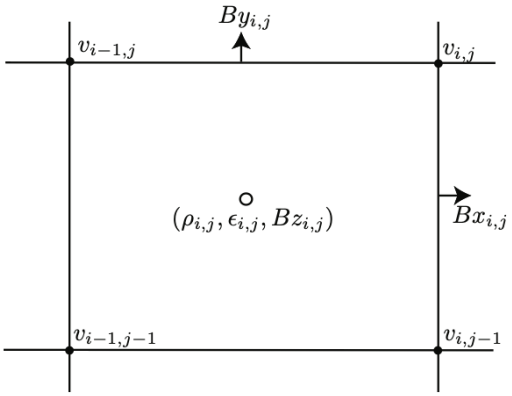

Figure 4.1: The Staggered Grid used in Lare2d. [Arber et al., 2001]

4.2 Equilibrium

The main factor that has been investigated is the effect of curvature of a coronal loop on the period of trapped sausage mode oscillations. A straight loop can be modelled as a slab with a non-uniform density profile of the following form:

$$\rho\left(\frac{x}{a}\right) = (\rho_0 - \rho_e)\,\mathrm{sech}^2\left[\left(\frac{x}{a}\right)^q\right] + \rho_e, \tag{4.5}$$

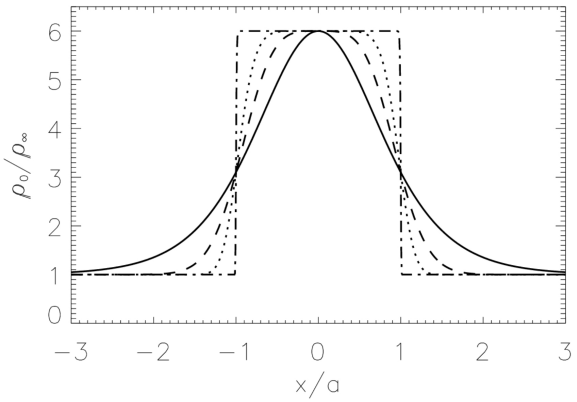

Figure 4.2: Symmetric Epstein profiles of the form given in equation (4.5) with the solid, dashed, dotted and dash-dotted curves corresponding to $q = 1, 2, 4, 100$ (effectively $q \to \infty$) respectively. [Nakariakov & Verwichte, 2005]

where ρ_0 is the maximum value of the density (when $x/a = 0$); ρ_e is the minimum value of the density (when $x/a \to \infty$); and q is a dimensionless parameter that affects the steepness of the curve, as is demonstrated in Figure 4.2.

This type of density profile is known as the symmetric Epstein profile [Nakariakov & Roberts, 1995] and models a magnetic flux tube embedded in a magnetised plasma with a thin boundary layer with an approximately linear variation of density and magnetic field strength between the internal and external values. As q is increased, the steepness of the transition between the internal and external densities increases, and the effective width of the edge layer decreases.

The magnetic field is in the y-direction, analogous to the variation of the density, with the form

$$B_y\left(\frac{x}{a}\right) = (B_0 - B_e)\,\mathrm{sech}^2\left[\left(\frac{x}{a}\right)^q\right] + B_e, \tag{4.6}$$

where B_0 is the magnetic field strength when $x/a = 0$; B_e is the value of the magnetic field strength when $x/a \to \infty$; and $B_e > B_0$. The magnetic field in the x-direction and z-direction is set as $B_x, B_z = 0$. The magnetic field is taken to be a 3D Cartesian vector field with elements as follows: $\mathbf{B} = (B_x, B_y, B_z)$.

The temperature of the plasma T can then be found from the pressure balance condition,

$$P_0 + \frac{B_0^2}{2\mu_0} = P_e + \frac{B_e^2}{2\mu_0}, \tag{4.7}$$

and the equation of state

$$P = \frac{\rho}{0.5 m_f} k_b T, \tag{4.8}$$

where P_0 is the internal gas pressure; P_e is the external gas pressure; m_f is the average mass of an ion, taken as 1.2 proton masses; and k_b is the Boltzmann constant.

The external plasma-β is small (~ 0.01 for the example case discussed in Section 5.1) outside the loop, which reflects the low plasma-β environment found in the solar corona. This set-up allows the value of internal plasma-β (calculated with equation 3.7) to be manipulated easily, although it has been shown to have a negligible effect on the periods of global sausage oscillations, with variation of $\sim 5\%$ across the range $0 < \beta_0 < 1$. [Inglis et al., 2009]

In order to produce an equivalent initial set-up for a curved coronal loop, similar Epstein profiles are used, but with their argument based around the radial distance from the origin, r. The radial Epstein profile for density is as follows:

$$\rho(x, y) = (\rho_0 - \rho_e) \operatorname{sech}^2 \left[\left(\frac{r(x, y) - r_0}{a} \right)^q \right] + \rho_e, \tag{4.9}$$

where $r(x, y) = \sqrt{x^2 + y^2}$; a is the minor radius of our coronal loop; and r_0 is the radial distance of the centre of the non-uniformity from the origin or the major radius of out coronal loop.

The magnetic field is given using a similar set-up to the case for a straight loop, again transforming to polar coordinates, but they are given using Cartesian coordinates as Lare2d takes its vector inputs in this form:

$$B_x(x, y) = \frac{y}{r(x, y)} \left((B_0 - B_e) \operatorname{sech}^2 \left[\left(\frac{r(x, y) - r_0}{a} \right)^q \right] + B_e \right), \tag{4.10}$$

$$B_y(x, y) = \frac{-x}{r(x, y)} \left((B_0 - B_e) \operatorname{sech}^2 \left[\left(\frac{r(x, y) - r_0}{a} \right)^q \right] + B_e \right), \tag{4.11}$$

$$B_z(x, y) = 0. \tag{4.12}$$

The major radius of the loop, r_0, was set as 7.5 Mm to give a loop length, L, of ~ 23.6 Mm which is similar the approximate length of the coronal loop used in the observational example of sausage mode oscillations used by Nakariakov et al. [2003]. The value of $B_e = 100$G was chosen for the same reason.

The boundary conditions of the simulation space that are in contact with the non-

uniformity are analogous to the footpoints of the coronal loop being modelled. These boundary conditions have been set as line-tied, meaning that the magnetic field is fixed at the boundary and all velocities are reflected. This results in a completely vertical magnetic field at the bottom of the computational region.

One potential issue with using line-tied boundary conditions at the base of the simulation is that any leaky modes that travel towards to simulation origin ($r = 0$) will be reflected back towards the loop structure itself when they meet the boundary. This means that any leaky modes which are excited will be reflected back towards the loop. This was considered to be acceptable as the amplitude of any leaky modes will be much smaller than any trapped ones, meaning our results shouldn't be affected.

This however, is not something that would occur in physical observations as when these leaky modes reach the solar surface they can be scattered in all directions, not just directly back towards the coronal loop. This is merely an artifact of the choice to use a 2.5D simulation, rather than a full 3D simulation. The effects of this and the possibilities for future development are discussed further in Section 6.

The boundary conditions at the remaining three edges of the computational box are damped, as although any leaky modes that are excited are likely to be low in amplitude it is still preferable to be able to remove these potential outside effects where possible.

In order to find an approximate equilibrium system in which to excite the sausage mode oscillations, this initial system is left to run until the kinetic energy in the system has reached less than 100 times its maximum value in what we will call the relaxation process.

Figure 4.3 illustrates this relaxation process by showing the potential energy (red) and the kinetic energy (blue) dropping to approximately 0 over time, allowing us to say that the new system after this process is in equilibrium. It is this equilibrium that is then excited with a driver, described in Section 4.3.

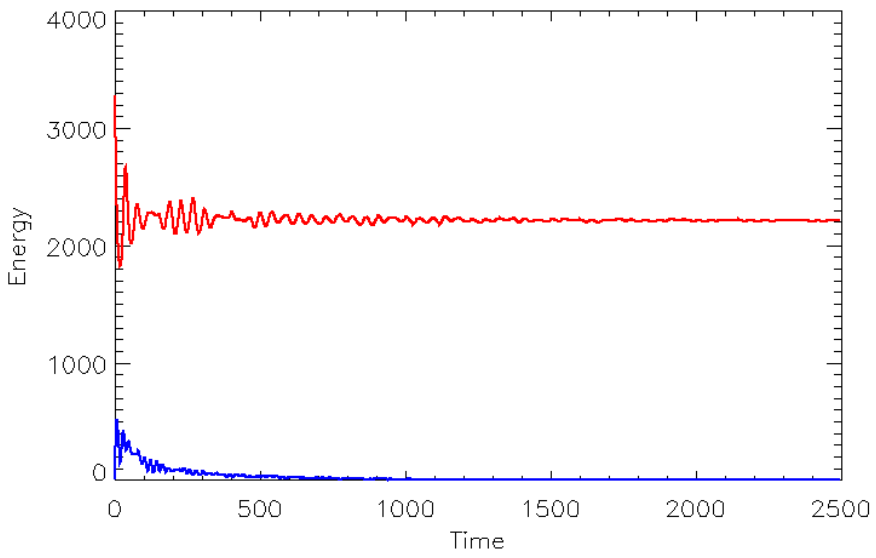

Figure 4.3: The kinetic energy (blue) and potential energy (red) within the computational area of the simulation during the relaxation process. Taken from the initial set-up at time $t = 0$ until the kinetic energy of the system was deemed to be low enough for the system to be considered as in equilibrium. For the case when $\rho_0/\rho_e = 80$ and $a/r_0 = 0.2$. All quantities are shown in normalised units described in Table 4.1.

Figures 4.4a - 4.4d show the characteristics of the equilibrium reached after the relaxation process has concluded. Examining figures 4.4a - 4.4c, it is clear that they haven't deviated significantly from the set-up described in equations 4.5 - 4.12 in their radial and azimuthal characteristics and as such, we will continue to use these. Figure 4.4d shows that the peak value of the density, ρ_0, is lower for the equilibrium (red) than in the initially prescribed setup (blue); the value of the external density, ρ_e, is relatively unchanged; and the vertical position of the centre of the coronal loop, r_0, has shifted slightly and as such these new equilibrium values are taken when performing all calculations.

We will also approximate the angular shape of the coronal loop as an ellipse with a horizontal semi-major radius of $r_{0,i}$ as the value of r_0 used in the initial set-up; and a vertical semi-minor radius of $r_{0,e}$ as the value of r_0 found in the equilibrium state after the relaxation process. This is justified by the line-tied boundary conditions preventing the footpoints of the loop from moving. Thus, the horizontal displacement of the loop from the origin along the x-axis cannot change.

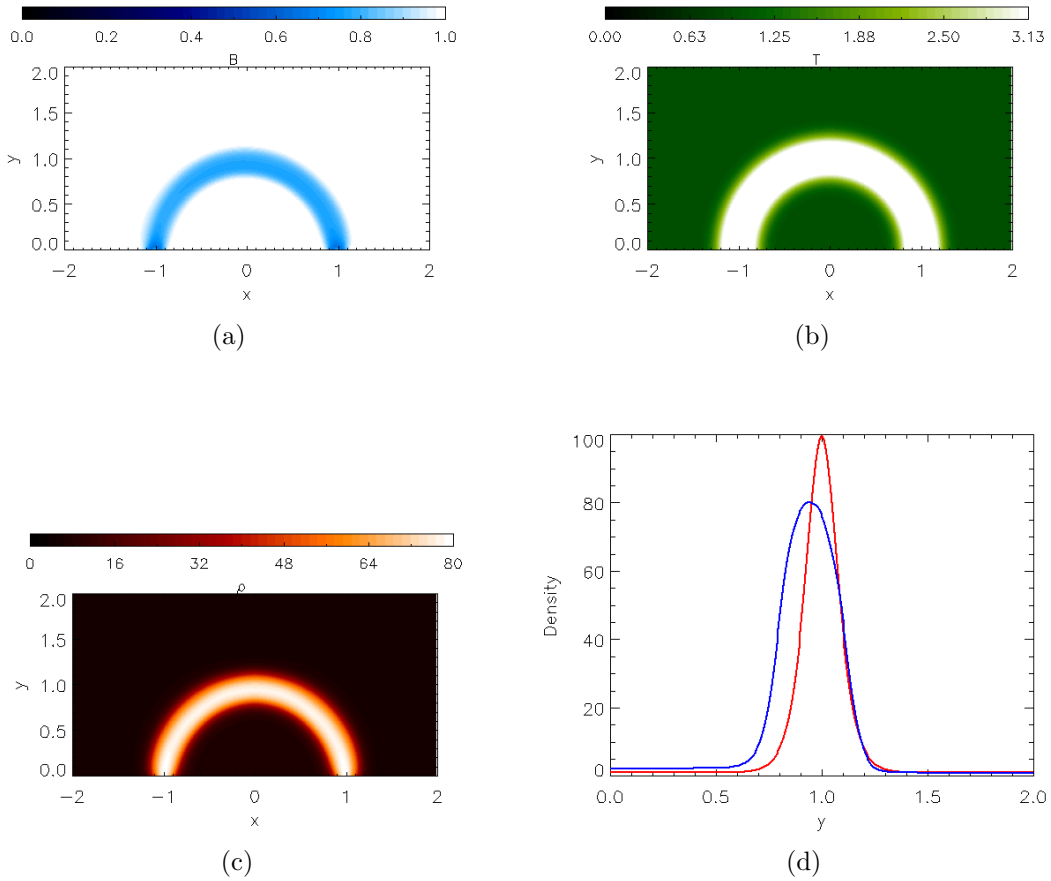

Figure 4.4: Subfigures (a)-(c) show the different properties of the Equilibrium set-up through the process described in section 4.2 for the case where $\rho_0/\rho_e = 80$ and $a/r_0 = 0.2$. The properties shown are magnetic field (a); temperature (b); and the density (c). Density as a function of distance along a vertical slit at $x = 0$ for the initial conditions (red) and the relaxed equilibrium (blue) (d). All quantities are shown in normalised units described in Table 4.1.

4.3 Excitation

The sausage mode oscillations are excited by introducing a velocity pulse to this approximate equilibrium system, based on a Gaussian derivative function, and in the curved loop takes the following form:

$$u_x = u_{\max}\frac{r_{0,e}\cdot x}{r(x,y)}\left\{\frac{r(x,y)-r_{0,i}}{a_v}\exp\left[-\left(\frac{r(x,y)-r_{0,i}}{a_v}\right)^2\right]\right\}\mathrm{M_n}(\theta(x,y)), \tag{4.13}$$

$$u_y = u_{\max}\frac{r_{0,e}\cdot y}{r(x,y)}\left\{\frac{r(x,y)-r_{0,i}}{a_v}\exp\left[-\left(\frac{r(x,y)-r_{0,i}}{a_v}\right)^2\right]\right\}\mathrm{M_n}(\theta(x,y)), \tag{4.14}$$

where a_v is the width of this velocity pulse; u_x and u_y are the elements of the velocity vector, $\mathbf{u} = (u_x, u_y, 0)$; $\theta(x,y)$ is the angular position with respect to the origin, calculated as $\theta(x,y) = \arctan2(x,y)$; and $\mathrm{M_n}(\theta)$ is a function that describes which harmonic (if any) of the sausage mode oscillations are to be excited. If the n-th harmonic is desired, then it should be set as $\mathrm{M_n}(\theta) = \sin(\theta/n)$. However, if a form is required that is not a pure harmonic, then $\mathrm{M_n}(\theta)$ can be replaced with angular dependence functions of other forms. Figure 3.3 illustrates the first harmonic of a sausage mode, which is modelled using $\mathrm{M_1}(\theta)$ within equations (4.13) and (4.14). Small values for $u_{\max}$ were used in order to approximate the linear regime.

4.4 Normalisation Constants

As discussed in Section 4.1, Lare solves normalised MHD equations with three normalisation constants set by the user ($\widetilde{L}$, $\widetilde{B}$ and $\widetilde{\rho}$) and all other normalisation constants are derived from these. These normalisation constants were chosen to allow easy description and interpretation of experiments performed with the equilibrium set-up described in Section 4.2. $\widetilde{L}$ was chosen to be the initial major radius of the loop structure $r_{0,i}$; $\widetilde{B}$ was chosen to be the external magnetic field, B_e; and $\widetilde{\rho}$ was chosen to be the external mass density, ρ_e. Their values and some derived normalisation constants are given in Table 4.1.

Parameter	Value	Unit
$\widetilde{L}$	7.5	Mm
$\widetilde{B}$	0.01	T
$\widetilde{\rho}$	2×10^{-12}	kg m^{-3}
$\widetilde{t}$	1.189	s
$\widetilde{T}$	5780	MK

Table 4.1: The normalisation constants used throughout the rest of this thesis.

4.5 Convergence Test

In order to choose a size for the numerical domain that was used in the simulation, a convergence test was performed on the case where $a = 0.2$ and $\rho_e = 80$. The period of oscillation in density at the loop apex was measured and the results of this convergence test are detailed in table 4.2. A numerical domain with 2000×2000 grid points was selected as a result and was used through all numerical simulations.

Grid Points	Period
500×500	7.3
1000×1000	7.6
1500×1500	7.8
2000×2000	7.9
2500×2500	7.9
3000×3000	7.9

Table 4.2: Results of the convergence test to find the appropriate number of grid points using the period of the global sausage mode of a curved coronal loop.

Chapter 5

Results

5.1 Example Case Analysis

We will choose one example case in order to demonstrate the process that was used to collect data from these numerical simulations before going on to present the results that were gathered. Our example case is that with the physical properties given in table 5.1.

Parameter	Value
r_0	1
a	0.2
ρ_e	1
ρ_0	100
B_e	1
B_0	0.95
q	1
n	1

Table 5.1: Selected properties of the coronal loop modelled in the example case.

A probe was placed at the loop apex ($x = 0$, $y = r_{0,e}$) and the density was measured at this point over time. The time series produced by this method for the example case is shown in Figure 5.1, along with its Fourier Power Spectrum in Figure 5.2. This method of finding the period of the global sausage mode is justified for two reasons: the global mode has an anti-node at the loop apex, meaning that the amplitude at the apex should be the largest of anywhere along the loop; and sausage oscillations do not perturb the loop axis so the probe does not need to move to remain at the apex.

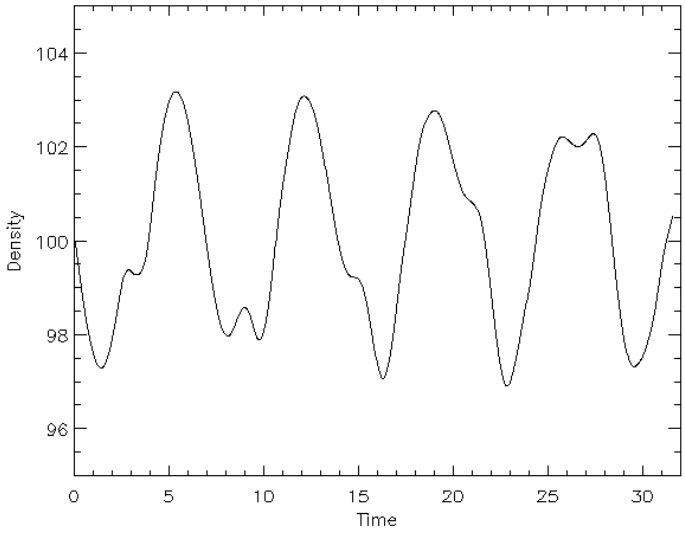

Figure 5.1: Density against time, taken at a point at the apex of the loop. Physical parameters of the case taken are given in Table 5.1.

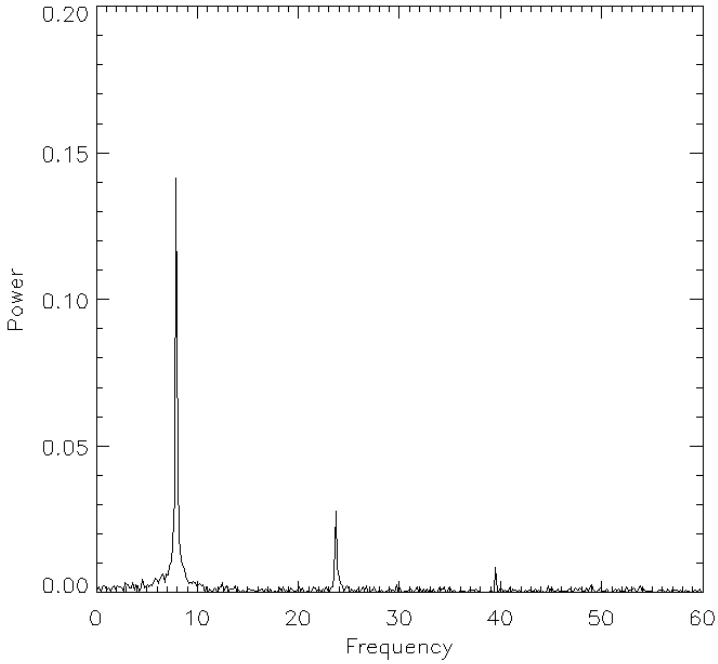

Figure 5.2: The Fourier Power Spectrum of the time series shown in Figure 5.1.

In order to verify that the oscillations observed were in fact trapped sausage modes a time-distance series for density was produced along a vertical slit in the y-direction along the line $x = 0$. This time-distance series was then time differenced - with the previous frame's value of density subtracted from the current frame - which is shown in Figure 5.3. This time-difference process was necessary to aid with visualisation, as the density perturbations are small compared to the magnitude of the maximum density ($\sim 3\%$).

Figure 5.3 helps to confirm that we are in the trapped regime as there is no visible density variation outside of the coronal loop. This reinforces the assumption made in Section 4.2 that the amplitude of any leaky modes reflecting off the boundaries will be very small. Also, the brightenings and darkenings at the edges of the coronal loop being in phase with each other and in antiphase with those at the loop centre is characteristic of sausage mode oscillations. This, along with the lack of perturbation to the loop axis, confirms that sausage mode oscillations have indeed been excited.

It is however clear from Figures 5.1 - 5.3 that higher harmonics have been excited, as well as the fundamental. This is likely due to a the loop not being exactly elliptical, as was assumed when setting up the exciting velocity pulse. Potential third and fifth harmonics are visible in the Fourier Power Series with even numbered harmonics absent. This is expected as even harmonics have nodes at the loop apex and odd harmonics have anti-nodes in this position.

The measured quantity extracted from these results is the frequency (and hence the period) of the global sausage mode oscillation, taken to be the lowest frequency spike in the Fourier Power Series. The error value on this measurement was calculated with the Full Width at Half Maximum (FWHM) of the peak.

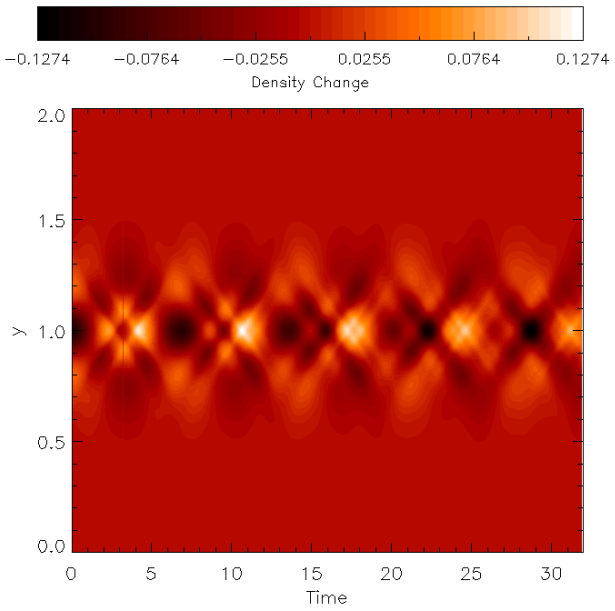

Figure 5.3: A time differenced series taken of a time-distance plot along a vertical slit at $x = 0$ showing density changes over time. Physical parameters of the case taken are given in Table 5.1.

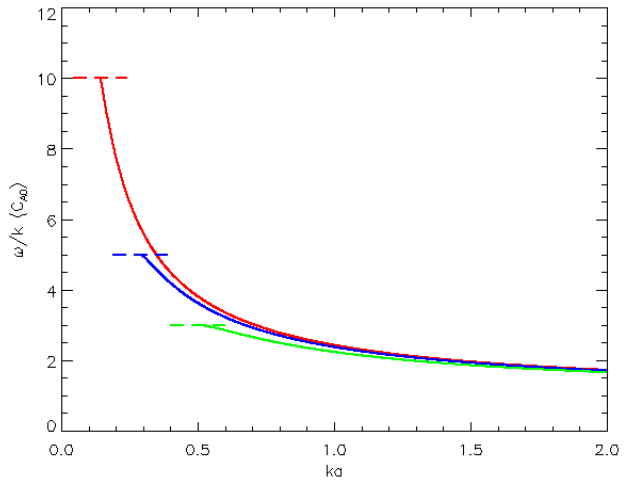

Figure 5.4: Phase speed - in units of internal Alfvén speed - as a function of normalised wavenumber for different density contrasts: the red line corresponds to $\rho_0/\rho_e = 100$; the blue to $\rho_0/\rho_e = 25$; and the green to $\rho_0/\rho_e = 9$. The dashed lines show the value of the external Alfvén speed for each density contrast.

5.2 Parametric Study

The theoretical frequencies (and periods) for a straight loop modelled as a magnetic slab can be calculated using equation 3.16. Three solutions for different density contrasts are plotted in Figure 5.4. It is worth noting that as r remains fixed between each experiment, k is also a fixed quantity. This allows easy visualisation of the relationship between the loop minor radius and the frequency of oscillation. The horizontal dashed lines represent the maximum value of phase speed for each case (equivalent to the external Alfvén speed, C_{Ae}). This maximum phase speed occurs at a cut-off value of ka, which is discussed in more depth in Section 3.3. As k is fixed this gives rise to a cut-off value of the minor radius in the straight slab model, a_c, below which the sausage oscillations are no longer trapped and we enter the leaky regime.

In order to perform the other experiments two parameters were varied independently of each other. These parameters are the density contrast, ρ_0/ρ_e, and the minor radius of the loop, a. All other parameters remained the same as those detailed in table 5.1.

Sixteen separate experiments were performed, with four values for a (0.2, 0.3, 0.4, and 0.5) and four values for ρ_e/ρ_0 (100, 80, 60, and 40). For each experiment, analysis was performed in the same fashion as for the example case show in in Section 5.1. Thus the frequency and period of the global sausage mode in these curved coronal loops was able to be calculated.

These results are plotted as crosses in Figures 5.5 and 5.6, alongside the theoretical solutions for a straight slab model of a coronal loop with the same plasma parameters represented by the solid red line. Again, the dashed horizontal line represents the maximum phase speed and makes clear the cut-off value of ka.

It can be seen that for curved loops with a small minor radius (that is larger than the cut-off value) that the frequencies and periods match closely to those from the straight slab model. A good example of this is the experiment with $\rho_0/\rho_e = 100$ and $a = 0.2$, as seen in Figures 5.5a and 5.6a.

However, for wider curved loops it can be seen that the frequency tends to be slightly higher (and hence the periods slightly lower) than would be expected using the straight slab model. The maximum deviation from the straight slab model in the experiments performed was around 10%. An example of one of these cases is the experiment with $\rho_0/\rho_e = 40$ and $a = 0.5$, as seen in Figures 5.5d and 5.6d.

There are two experiments in particular that lie very close to, or below, the theoretical cut-off value for the minor radius a_c. These are the experiments with $\rho_0/\rho_e =$

60 and $a = 0.2$; and $\rho_0/\rho_e = 40$ and $a = 0.2$. This places them no longer fully within the trapped regime, meaning that some of the assumptions made in the modelling of the coronal loop are invalid, and giving rise to some difficulty in taking results.

The amplitude of any leaky modes is no longer negligible, meaning that reflections from the computational boundaries interfere with the oscillations measured at the loop apex. The fact that there are leaky modes means that the oscillations measured at the loop apex are damped. Both of these factors reduce the number of periods of oscillation that can be measured, resulting in larger errors. However, changes discussed in Section 6.2 would help to alleviate these issues and make investigation of the leaky regime more possible.

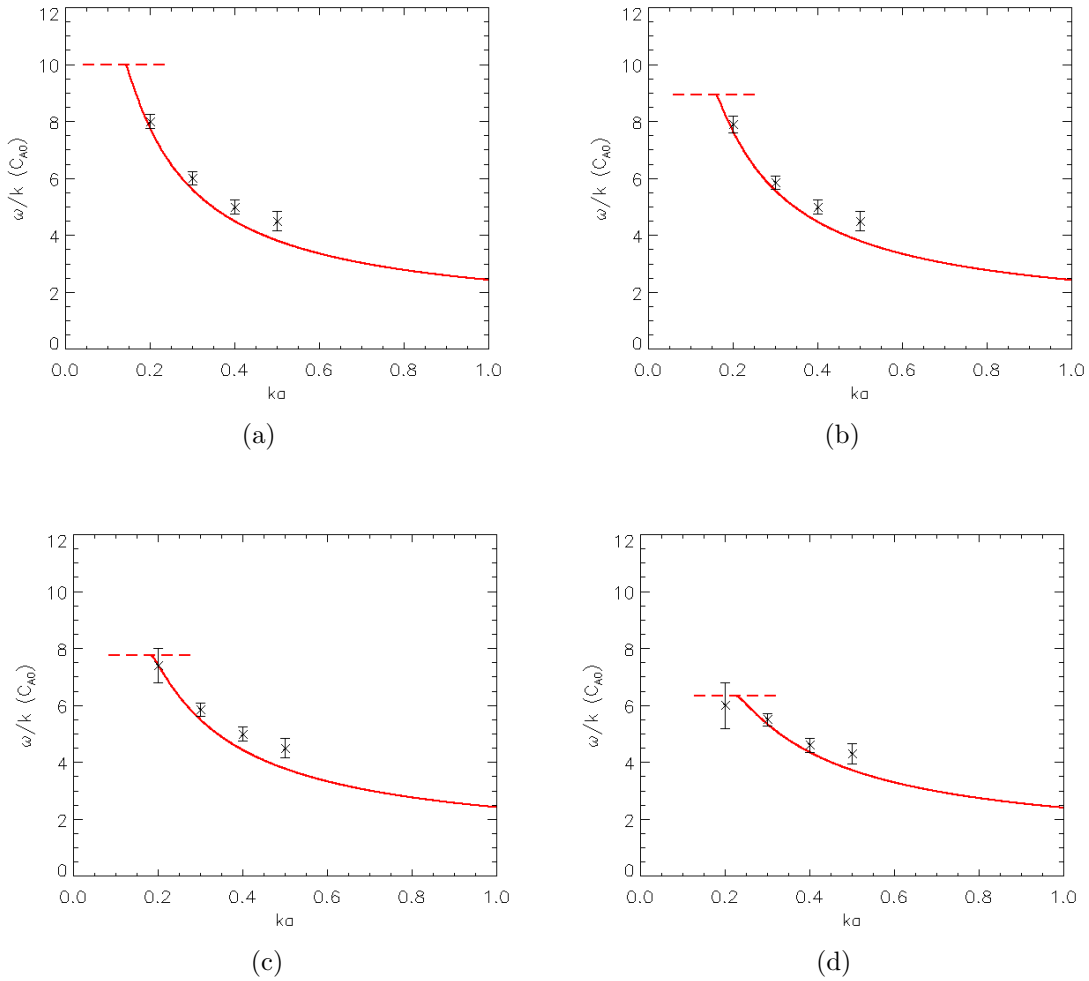

Figure 5.5: Phase speed - in units of internal Alfvén speed - as a function of normalised wavenumber at different density contrasts. The solid red lines represent the analytical solution for a straight, Epstein profile loop; the dashed lines show the value of the external Alfvén speed; and the crosses represent numerical data from simulations of a curved coronal loop modelled as a slab. (a) corresponds to $\rho_0/\rho_e = 100$; (b) to $\rho_0/\rho_e = 80$; (c) to $\rho_0/\rho_e = 60$; and (d) to $\rho_0/\rho_e = 40$.

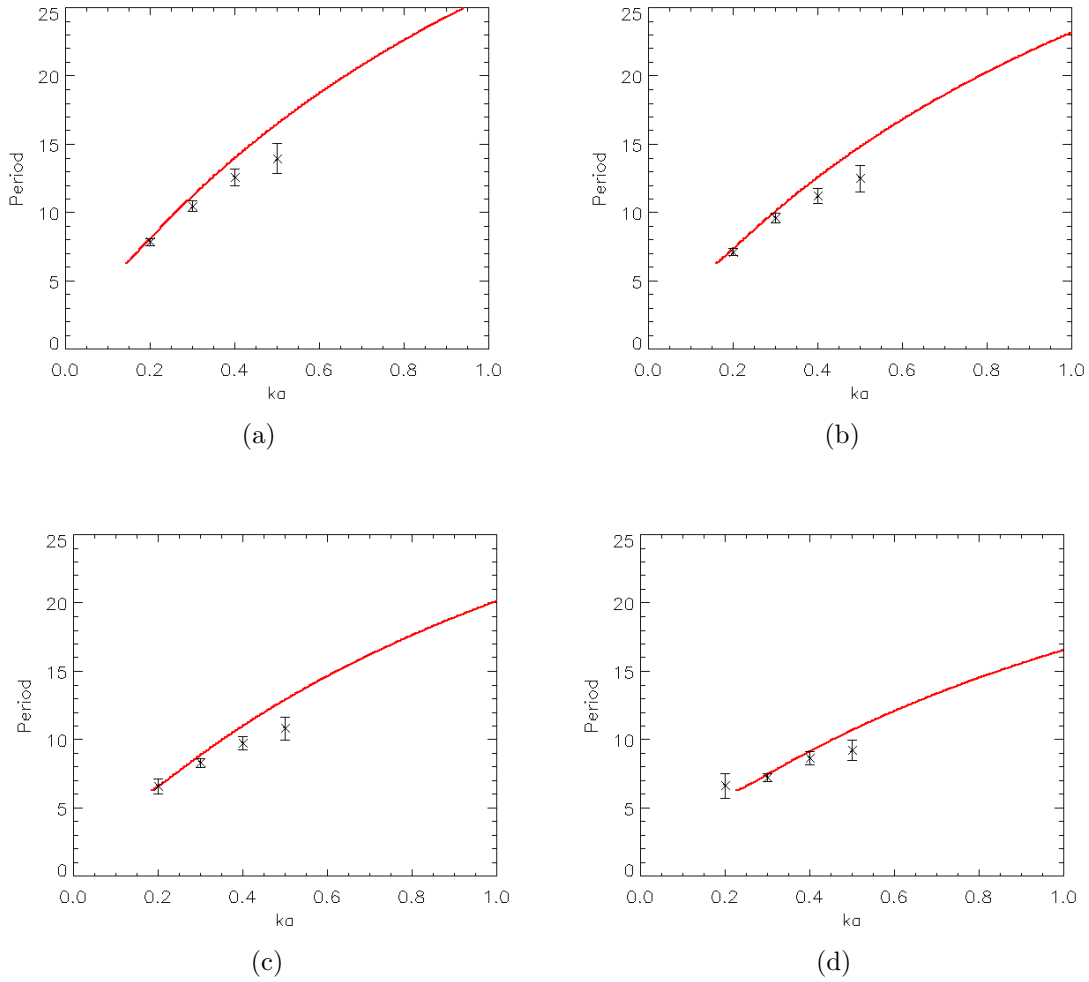

Figure 5.6: Period as a function of normalised wavenumber at different density contrasts. The red lines represent the analytical solution for a straight, Epstein profile loop; and the crosses represent numerical data from simulations of a curved coronal loop modelled as a slab. (a) corresponds to $\rho_0/\rho_e = 100$; (b) to $\rho_0/\rho_e = 80$; (c) to $\rho_0/\rho_e = 60$; and (d) to $\rho_0/\rho_e = 40$.

Chapter 6

Discussion

6.1 Discussion of Findings

An equilibrium setup has been found that approximates the structure of a coronal loop including the effects of curvature, as is shown in Figure 4.4. This equilibrium can be manipulated to model loops with different major radii, minor radii, density contrasts, and radial density profiles. This equilibrium is capable of supporting global sausage mode oscillations, which is illustrated in Figures 5.1 - 5.3. The velocity pulse used to excite the sausage mode oscillations can be customised to excite higher harmonics. The code used to produce these numerical experiments is written in such a way to be valuable for further investigation of the effects of many different parameters on sausage mode oscillations within a curved coronal loop.

Within this thesis it has been demonstrated that there is a measurable effect due to curvature when modelling sausage oscillations. For suitably thin coronal loops that remain within the trapped regime, the straight slab model is valid when investigating the global sausage mode. However, when considering thicker coronal loop structures, it would appear that the curvature of the structure has a non-negligible effect on the period of the global sausage mode. This effect was found to cause a maximum deviation of approximately 10% from the straight slab model, within the parameter range investigated.

A possibility of accounting for the effects of curvature in the modelling of fast magnetoacoustic sausage oscillations of coronal loops is shown. It is hoped that this work will contribute to further studies and investigations of the effects of curvature in coronal loops and will ease the implementation of these studies.

6.2 Future Work

Further experiments of the style presented within this work would be valuable in order to build a full picture of the dependence of the global trapped sausage mode period on the parameter space described (ρ_e/ρ_0, a). This work could be completed with more computing time and by making minimal changes to the code used within the experiments detailed in Section 5.2.

Of particular interest for further investigation would be the leaky regime for sausage mode oscillations within a curved coronal loop. This would require damping to be applied to the computational boundaries at $x = \pm 2$ and $y = 4$. Damping could not be applied to the full $y = 0$ boundary however, as this would affect the reflection at the loop footpoints and their line-tied boundary conditions. Instead, damping could be applied to the boundary everywhere apart from the loop footpoints, with $|x| < r - a$ and $|x| > r + a$ at $y = 0$.

This would allow the decay of the oscillations at the loop apex to be measured without interference by reflections from the boundaries. The outputs could then be the period, damping time, and associated quality factor. Hence the cut-off value of the minor radius could be investigated for the transition between the trapped and leaky regimes.

As higher harmonics of the sausage oscillation have shorter wavelengths (and hence larger wavenumbers), their cutoff values of a_c are smaller. This allows the investigation of the interaction between the leaky fundamental harmonic and trapped higher harmonics within the same coronal loop structure (this may be achieved by setting different values of n in Equations 4.13 and 4.14). It may also be valuable to investigate the form of the oscillations in the θ-direction by placing probes at different points along the loop axis and performing analysis of the oscillation amplitudes at each point.

Bibliography

Antolin, P., & Van Doorsselaere, T. 2013, Astronomy and Astrophysics, 555, 1

Arber, T. D., Longbottom, A. W., Gerrard, C. L., & Milne, A. M. 2001, Journal of Computational Physics, 171, 151

Carley, E. P., Hayes, L. A., Murray, S. A., et al. 2019, Nature Communications, 10, 1

Chen, S. X., Li, B., Xia, L. D., & Yu, H. 2015, Solar Physics, 290, 2231

Cooper, F. C., Nakariakov, V. M., & Williams, D. R. 2003, Astronomy and Astrophysics, 409, 325

Edwin, P. M., & Roberts, B. 1982, Solar Physics, 76, 239

—. 1983, Solar Physics, 88, 179

Gruszecki, M., Nakariakov, V. M., & Van Doorsselaere, T. 2012, Astronomy and Astrophysics, 543, doi:10.1051/0004-6361/201118168

Hapgood, M., & Thomson, A. 2010, Space Weather: Its impact on Earth and implications for business, Tech. rep.

Inglis, A. R., Van Doorsselaere, T., Brady, C. S., & Nakariakov, V. M. 2009, Astronomy and Astrophysics, 503, 569

Kaneda, K., Misawa, H., Iwai, K., et al. 2018, The Astrophysical Journal, 855, L29

Mészárosová, H., Rybák, J., Kashapova, L., et al. 2016, Astronomy and Astrophysics, 593, 1

Mossessian, G., & Fleishman, G. D. 2012, Astrophysical Journal, 748, doi:10.1088/0004-637X/748/2/140

Nakariakov, V. M., Anfinogentov, S., Storozhenko, A. A., et al. 2018, The Astrophysical Journal, 859, 154

Nakariakov, V. M., Melnikov, V. F., & Reznikova, V. E. 2003, Astronomy and Astrophysics, 412, 10

Nakariakov, V. M., & Roberts, B. 1995, Solar Physics, 159, 399

Nakariakov, V. M., & Verwichte, E. 2005, Living Reviews in Solar Physics, 2, doi:10.12942/lrsp-2005-3

Nakariakov, V. M., Pilipenko, V., Heilig, B., et al. 2016, Space Science Reviews, 200, 75

Pascoe, D. J., & Nakariakov, V. M. 2016, Astronomy and Astrophysics, 593, 1

Sigmund, O., & Petersson, J. 1998, Structural Optimization, 16, 68

Tian, H., Young, P. R., Reeves, K. K., et al. 2016, The Astrophysical Journal, 823, L16

Van Doorsselaere, T., De Groof, A., Zender, J., Berghmans, D., & Goossens, M. 2011, Astrophysical Journal, 740, doi:10.1088/0004-637X/740/2/90

Yu, S., Nakariakov, V. M., Selzer, L. A., Tan, B., & Yan, Y. 2013, Astrophysical Journal, 777, doi:10.1088/0004-637X/777/2/159